Progress in the Application of an Aerodynamic Shape Optimization Capability using Hybrid Laminar Flow Control to Airfoils and Infinite Swept Wings

Justin M. Pascual [*] and David W. Zingg [†]

Institute for Aerospace Studies, University of Toronto, ON M3H 5T6

The use of hybrid laminar flow control can extend the region of laminar flow on a wing at sweep angles and Reynolds numbers beyond those for which natural laminar flow is effective. In this paper, a suction boundary condition implemented in a Reynolds-averaged Navier-Stokes aerodynamic shape optimization framework coupled with the SA-sLM2015cc local correlation-based transition model is applied to lift-constrained drag-minimization of airfoils and wings. The transition location was determined for a supercritical airfoil, after which suction was applied upstream of this location. After determining the resulting transition location on the upper surface, suction is applied upstream of the new location while retaining the original suction location. By adding a second suction location at this new transition location, further drag reductions were obtained, indicating the successful application of multiple suction locations at varying suction velocities. The airfoil is then optimized with suction applied upstream of the baseline transition location, yielding a higher drag reduction compared to the optimization without the application of suction. Additionally, the airfoil was optimized without suction and the suction boundary condition was then applied upstream of the new transition location. These results indicated that the application of suction to an optimized geometry yields a higher drag reduction compared to the case where suction is applied to the baseline geometry, which is then optimized. To investigate the effect of suction on crossflow instabilities, an infinite swept wing is tested with suction added upstream at a single location on the upper surface, lower surface and both surfaces. This geometry was optimized with and without suction, and the results with suction yielded a higher drag reduction compared with those without. In contrast to the airfoil case without sweep, on the infinite swept wing when suction is applied to a geometry optimized without suction, the drag reduction is lower. These results demonstrate that the presented approach to modelling suction and transition provides a promising methodology to study and optimize wings for hybrid laminar flow control.

I. Nomenclature

A	=	airfoil area
c	=	chord
C_D	=	coefficient of drag
C_L	=	coefficient of lift
e	=	total energy per unit volume
$\mathbf{\hat{E}}$	=	inviscid flux vector in the ξ-direction
$\mathbf{\hat{E}_v}$	=	viscous flux vector in the ξ-direction
J	=	metric Jacobian
M	=	Mach number
Pr	=	Prandtl number
$\mathbf{Q}$	=	conservative flow variables at individual node
Re	=	Reynolds number

---

*PhD Student, University of Toronto Institute for Aerospace Studies, AIAA Student Member, justin.pascual@mail.utoronto.ca

†Distinguished Professor of Computational Aerodynamics and Sustainable Aviation, University of Toronto Institute for Aerospace Studies, AIAA Associate Fellow, david.zingg@utoronto.ca

v_{suc} = suction speed
V_∞ = free-stream velocity
Λ = sweep angle
ρ = density
ξ = curvilinear coordinate

II. Introduction

THE commercial aviation industry has seen substantial growth over the past few decades, and setting aside the reduction in travel during the COVID-19 pandemic, the demand for safe and efficient travel has increased by roughly 6% each year [1]. With this increase in demand come increased environmental concerns, resulting in growing interest in developing more efficient aircraft designs [1]. To aid the development of these designs, aerodynamic shape optimization iteratively performs simulations and uses the results to optimize the design for specific performance parameters, creating a more efficient workflow compared with cut-and-try design methods.

With a typical commercial aircraft, viscous drag, contributes roughly 50% of the overall drag at cruise [2]. As the flow transitions from laminar to turbulent, the friction increases and the boundary layer thickens, thereby increasing the overall drag. To delay this transition to turbulence, flow control methods can be employed to shift the transition location aft [3]. The flow transitions on swept wings mainly by two mechanisms, the first being Tollmien-Schlichting (TS) instabilities, which occur in two-dimensional boundary layers in vortices aligned with the spanwise direction. TS instabilities are advected downstream, are highly receptive to disturbances in the flow, and are amplified as they move downstream, resulting in the flow transitioning to turbulent flow [4]. The second mechanism is crossflow (CF) instabilities which arise on swept wings when there is an inflection point in the transverse velocity profile. This inflection point makes the flow unstable, resulting in streamwise vortices that transition the flow from laminar to turbulent.

With the goal of delaying the transition from laminar to turbulent flow, a promising method of increasing aerodynamic efficiency is natural laminar flow (NLF), a passive technique which uses wing shaping to extend the region of laminar flow. The design challenges that NLF faces are the conflicting requirements required to suppress both TS and CF instabilities. For example, favourable pressure gradients suppress TS instabilities but amplify CF instabilities. Furthermore, by increasing the sweep angle of the wing, wave drag is reduced, but the crossflow instabilities dominate, contributing to increased viscous drag. These trade-offs involving conflicting pressure gradients and sweep angles result in NLF being limited to modest sweep angle and Reynolds number applications [5, 6].

For combinations of high sweep angle and Reynolds number, active laminar flow control techniques must be used. Hybrid laminar flow control (HLFC) combines the wing shaping aspect of NLF and applies small amounts of suction. In combination with shaping, the suction affects the boundary-layer profiles to delay transition. The best candidates for this technique are the wings and empennage because of their large wetted area and typically high sweep, with the the nacelles and other surfaces still being considered for other drag reduction techniques [7].

The concept of using suction across the entirety of both the upper and lower surfaces of the wing was investigated by NASA in the NASA Langley Laminar-Flow-Control Experiment [8–11]. The experiment used a supercritical airfoil (in both unswept and swept configurations), with the goal being to validate transition prediction theories and to compare the relative merit of slotted and perforated suction surfaces. The experiments successfully demonstrated that the implementation of suction was able to move the transition location back to 60% of the chord, and validated that both the slotted suction and perforated surface configurations are able to move the transition location downstream.

Building on these tests, Fisher and Fischer demonstrated the effectiveness and reliability of active laminar flow control on a JetStar airplane in the Leading-Edge Flight Test (LEFT) [12]. The LEFT test had the aircraft outfitted with the two aforementioned configurations (slots of suction and perforated surface with suction) along with experimental attempts to protect the surface (including the suction system) from insect, ice and particulate contamination during takeoff, such as Krueger flaps with deicer nozzles. Both configurations were successfully implemented, with the slotted suction proving more effective at moving the transition location downstream. It was determined that the very small holes of the perforated surface were easily clogged.

Computationally, Sudhi et al. combined active laminar flow control implementation with aerodynamic shape optimization to a two-dimensional airfoil [13]. Using XFOIL, an aerodynamic solver coupled with an e^N transition prediction method, the transition location was determined. Drag-minimization optimizations were carried out with and without boundary-layer suction, where the onset of suction was used as a design variable to create an optimized suction profile. This optimized profile was applied upstream of the transition location, resulting in transition being delayed to 80% of the chord, with a drag reduction of 30% compared to the optimized design without suction.

The objective of the current work is to integrate boundary-layer suction into aerodynamic shape optimization for application to the design of swept wings. Our interest is in the reduction of drag through the optimization of suction velocity and location as well as the geometry, while providing a net decrease in power requirements. This work will be applicable to high-speed high-sweep aircraft, such as twin-aisle class aircraft and blended wing-body aircraft.

Section III describes the flow solver, transition prediction model, and aerodynamic shape optimization tools, including the active laminar flow control modelling. Section IV presents the results of lift-constrained drag minimization of two-dimensional airfoils with and without sweep incorporating suction in various ways. Finally, conclusions are presented in Section V.

III. Methodology

Aerodynamic shape optimization is performed using Jetstream, the University of Toronto Institute for Aerospace Studies' in-house, high-fidelity aerodynamic shape optimization framework. This framework includes five main components: a Newton-Krylov-Schur flow solver for the RANS equations [14],[15], an empirical local correlation-based transition prediction model coupled to the one-equation Spalart-Allmaras (SA) turbulence model [16],[17], an integrated geometry parameterization and linear-elasticity-based mesh deformation scheme [18], a gradient-based optimizer SNOPT used with the discrete-adjoint gradient method [19], and a free-form deformation (FFD) and axial deformation technique for geometry control [20]. Additionally, the active suction aerodynamic shape optimization capability is added via a suction boundary condition.

A. RANS Flow Solver

The flow solver, Diablo [14],[15], is a multiblock parallel implicit solver that uses second-order summation-by-parts (SBP) operators for spatial discretization and simultaneous approximation terms (SATs) [21] for implementing boundary and block interface conditions. SATs are penalty terms that enforce the boundary conditions to the specified target state. The SBP-SAT discretization of the governing equations produces a system of nonlinear equations, which is solved using Newton's method in two phases: an approximate-Newton phase and an inexact-Newton phase. During the approximate-Newton phase, an approximate Jacobian is used with the implicit Euler method, and the time step is gradually increased. In the inexact-Newton phase, the exact Jacobian is approximated through matrix-free matrix-vector products, in combination with a more rapid increase in the time step. The transition from the approximate-Newton phase to the inexact-Newton phase occurs when the total residual drops by five orders of magnitude. In both phases, the system of linear equations generated at each iteration is solved using the preconditioned Krylov iterative solver GMRES.

B. Transition Prediction Model

The flow solver includes the boundary-layer transition prediction capability using the SA-sLM2015cc model developed by Piotrowski and Zingg [16, 17, 22]. This model is based on the $\gamma - Re_{\theta t}$ model, an empirical local correlation-based model developed by Langtry and Menter [23] for modelling TS and CF instabilities. This model consists of two transport equations, one for γ, the intermittency function, and one for $Re_{\theta t}$, the momentum-thickness Reynolds number. The SA-sLM2015 transition prediction model is coupled with the one-equation Spalart-Allmaras turbulence model [24] and includes smoothing of non-smooth functions in the $\gamma - Re_{\theta t}$ model, ensuring a smooth design space. Piotrowski and Zingg further extended this to include compressibility corrections (cc) for TS and CF instabilities, resulting in the model designation SA-sLM2015cc [25].

C. Geometry Parametrization, Mesh Deformation, Geometry Control

The optimization framework consists of an integrated geometry parametrization and mesh deformation method developed by Hicken and Zingg [18]. Each computational grid block is associated with a B-spline volume, with the B-spline control points on the surface offering a low-dimensional approximation of the initial geometry. Using a linear-elasticity-based mesh deformation technique, adjustments to the surface control points propagate changes to the volume control mesh. Geometry control is achieved through a combination of free-form and axial deformation methods [20], wherein the free-form deformation (FFD) volumes are defined as B-spline volumes, and the axial curves are defined as B-spline curves. The FFD volume control points are used to control section shape, chord and twist, while the axial control curves are used to control sweep, span, and dihedral. The deformation of the axial control curves is not needed for the airfoil and infinite swept wing cases considered in this paper.

D. Gradient-Based Optimization

The optimization is performed using a gradient-based optimization algorithm, SNOPT [19], which uses a sequential quadratic programming framework and can handle both linear and non-linear constraints. Gradients are evaluated using the discrete-adjoint method [26, 27].

E. Suction Boundary Condition

To model suction along the wing surface, it is represented as a no-slip wall with a downward normal velocity. This adjustment involved modifying the parameters of the SAT for the no-slip adiabatic wall. Specifically, the momentum at the wall is modified to model suction. The solution vector, $\mathbf{Q}_{\text{target}}$, modified for the suction boundary condition is defined as:

$$\mathbf{Q}_{\text{target}} = \begin{bmatrix} \rho \\[4pt] \dfrac{\frac{\partial \xi}{\partial x} \cdot v_{\text{suc}} \cdot \rho}{\sqrt{\left(\frac{\partial \xi}{\partial x}\right)^2 + \left(\frac{\partial \xi}{\partial y}\right)^2 + \left(\frac{\partial \xi}{\partial z}\right)^2}} \\[20pt] \dfrac{\frac{\partial \xi}{\partial y} \cdot v_{\text{suc}} \cdot \rho}{\sqrt{\left(\frac{\partial \xi}{\partial x}\right)^2 + \left(\frac{\partial \xi}{\partial y}\right)^2 + \left(\frac{\partial \xi}{\partial z}\right)^2}} \\[20pt] \dfrac{\frac{\partial \xi}{\partial z} \cdot v_{\text{suc}} \cdot \rho}{\sqrt{\left(\frac{\partial \xi}{\partial x}\right)^2 + \left(\frac{\partial \xi}{\partial y}\right)^2 + \left(\frac{\partial \xi}{\partial z}\right)^2}} \\[20pt] e \end{bmatrix}, \tag{1}$$

where v_{suc} is the user-defined suction speed parameter and ξ is the curvilinear coordinate direction normal to the surface.

This value for $\mathbf{Q}_{\text{target}}$ is used in the following SATs to enforce a suction boundary condition. The inviscid portion of the SAT is defined as:

$$\text{SAT}_{\text{inv\_suction}} = -H_b^{-1} J^{-1} A_\xi^+ (\mathbf{Q} - \mathbf{Q}_{\text{target}}) \tag{2}$$

where H_b is the boundary node element of the diagonal norm matrix H, $\mathbf{Q}$ contains the flow variables in the current block, J is the Jacobian of the coordinate transformation, and

$$A_\xi^+ = \frac{A_\xi + |A_\xi|}{2}, \qquad A_\xi = \frac{\partial \hat{\mathbf{E}}}{\partial \hat{\mathbf{Q}}}.$$

An explanation of the curvilinear coordinate transformation and associated notation can be found in [28].

The overall form of the viscous SAT is defined as:

$$\text{SAT}_{\text{suction\_visc\_overall}} = \frac{H_b^{-1}}{Re} \left[\sigma^W (\mathbf{Q} - \mathbf{Q}_{\text{target}}) + \sigma^V \left(\hat{\mathbf{E}}_v - \hat{\mathbf{E}}_{v,\text{target}} \right) \right] \tag{3}$$

which consists of both a viscous surface penalty and a viscous flux penalty. The viscous surface penalty is defined as:

$$\text{SAT}_{\text{visc\_suction}} = \frac{H_b^{-1} \sigma^W}{Re} (\mathbf{Q} - \mathbf{Q}_{\text{target}}), \tag{4}$$

$$\sigma^W = -\frac{\xi_x^2 + \xi_y^2 + \xi_z^2}{J} \frac{\mu}{2\rho} \max\left(\frac{\gamma}{Pr}, \frac{5}{3} \right).$$

A viscous flux penalty is used to enforce the adiabatic condition. We use the value of $\hat{\mathbf{E}}_{v,\text{target}}$, equal to $\hat{\mathbf{E}}_v$ with the temperature derivative terms normal to the wall set to zero. $\hat{\mathbf{E}}_v$ and $\hat{\mathbf{E}}_{v,\text{target}}$ are defined in [14]. From this, we use a

viscous SAT defined as:

$$\text{SAT}_{\text{visc\_flux}} = \frac{H_b^{-1}\sigma^V}{Re}\left(\hat{\mathbf{E}}_v - \hat{\mathbf{E}}_{v,\text{target}}\right) \tag{5}$$

where $\sigma^V = 1$ at the low-side boundary and $\sigma^V = -1$ at the high-side boundary.

The inviscid portion of the SAT in Equation 2, the viscous surface penalty in Equation 4, and the viscous flux penalty in Equation 5 are used to enforce an overall suction boundary condition.

IV. Results

In this section, the free-transition optimization and suction boundary condition framework described in Section III is applied to airfoils (no sweep) and infinite swept wings (includes sweep). Cases are run at operating conditions to test the methodology with lower Reynolds numbers to provide a more optimal location for the application of suction (i.e. further downstream from the leading edge). These cases investigate the effectiveness of active flow control on translating the transition location downstream. This is done by varying the suction speed and suction extent and comparing the results of both flow evaluations and optimizations. These cases were chosen to develop and test the methodology and future work will address practical applications.

A. Airfoil Studies

The following cases were completed using the RAE2822 airfoil as the initial geometry for lift-constrained drag minimization, at $M = 0.6$, $Re = 10 \times 10^6$, $C_L = 0.42$, subject to geometric constraints specified in Section IV.A.3. This geometry has no sweep and therefore, there will be no crossflow instabilities in this case. The computational meshes for these airfoils are 300×122 O-grids.

1. Application of Suction at the Updated Transition Location

In order to determine a suitable location for the suction, we first solve the flow over the baseline geometry under the above conditions to find the location of transition on the upper and lower surfaces. The suction boundary condition is subsequently applied to 4 nodes on the upper surface, spanning approximately 2% of the chord upstream of the transition location. The case was then rerun with this suction location and analyzed for the new transition location. This process of adding suction upstream of the transition location on the upper surface was repeated, resulting in two suction locations, pushing the transition location further downstream. This process was executed with distinct suction velocities: $v_{\text{suc}} = 0.1\% \, V_\infty$ and $0.5\% \, V_\infty$, where V_∞ is the free-stream velocity.

The results of these flow evaluations are presented in Table 1. The accompanying coefficient of pressure and friction plots are shown in Fig. 1 which demonstrate that the transition location is pushed farther aft by the suction boundary condition. In Fig. 1a with a suction speed of $0.1\% \, V_\infty$, transition is pushed back 7% of the chord with a 6.2% reduction in drag for a single suction location and 15% of the chord with a 13.0% reduction in drag for two suction locations. Similarly, as shown in Fig. 1b, when the suction velocity is increased to $0.5\% \, V_\infty$, transition is pushed back 20% of the chord with a 14.1% reduction in drag for a single suction location and 30% of the chord with a 21.4% reduction in drag for two suction locations.

These results correlate with experimental evidence [11] that the application of a suction boundary condition upstream of the transition location is able to move the transition location farther aft, thereby reducing the overall drag. Unfortunately, the authors have not been able to find an available experimental dataset suitable for quantitative validation of the methodology for incorporating suction.

2. Application of Suction to a Previously Optimized Geometry

The suction boundary condition was also applied at a fixed location to a geometry obtained from a lift-constrained drag minimization without suction. A single-point optimization was performed at a target lift coefficient of 0.42 with an area constraint and minimum thickness constraints. The optimization problem can be summarized as

Table 1   Summary of results for sequential addition of suction applied to the upper surface of the airfoil while varying the suction speed.

Configuration	C_D (counts)	L/D	AOA
Baseline	54.45	77.13	1.34°
$v_{\text{suc}} = 0.1\% \, V_\infty$			
Suction at 21% x/c	51.06 (-6.22%)	82.27	1.30°
Added Suction at 28% x/c	47.38 (-13.00%)	88.65	1.26°
$v_{\text{suc}} = 0.5\% \, V_\infty$			
Suction at 21% x/c	46.80 (-14.05%)	89.75	1.24°
Added Suction at 34% x/c	42.78 (-21.43%)	98.17	1.19°

(a) $\mathbf{v_{suc}} = \mathbf{0.1}\% \, \mathbf{V_\infty}$ (b) $\mathbf{v_{suc}} = \mathbf{0.5}\% \, \mathbf{V_\infty}$
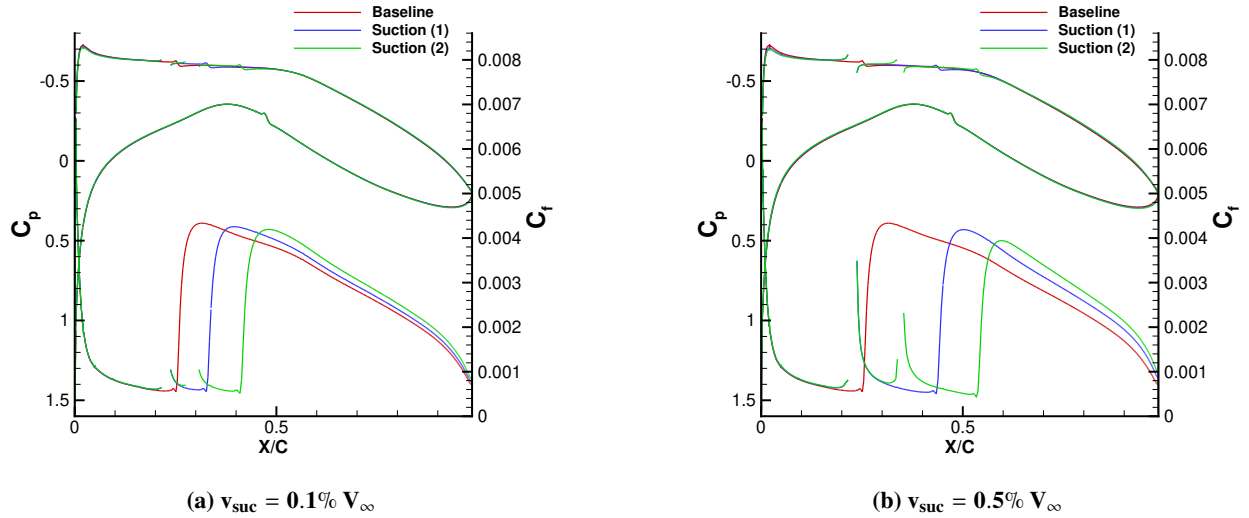
Fig. 1   Pressure and friction coefficient plots for cases involving the application of suction on the upper surface at the updated transition location while varying the suction speed. Suction (1) indicates that the suction boundary condition was applied at a single location on the upper surface. Suction (2) indicates that the suction boundary condition was applied at two locations; the original location and the updated transition location.

$$\begin{aligned}
\min_{\mathbf{X}} \quad & C_D(\mathbf{X}) \\
\text{s.t.} \quad & C_L = 0.42 \\
& A \geq A_{\text{baseline}} \\
& t/c \geq 0.15(t/c)_{\text{init}},
\end{aligned} \tag{6}$$

where $\mathbf{X}$ represents the design variable vector, C_L and C_D the lift and drag coefficients, respectively, C_L^* the target coefficient of lift, and t/c the thickness-to-chord ratio for each FFD control point pair. The 'init' subscript indicates the value of the quantity from the baseline geometry.

The chord length, leading edge, and trailing edge of the airfoil are fixed, while the angle of attack and section shape are allowed to vary. The transition location of the optimized airfoil was determined and suction was applied upstream at 57% of the chord on the upper surface. As shown in Table 2, the optimized geometry has a 44% reduction in drag compared to the baseline design, and Figure 2 shows that when a suction speed of $v_{\text{suc}} = 0.1\% \, V_\infty$ is applied at the new

6

Table 2   Summary of results for flow evaluations with suction applied at 57% of the upper surface to an optimized geometry. For these cases, the suction extent is fixed and the suction speed is varied.

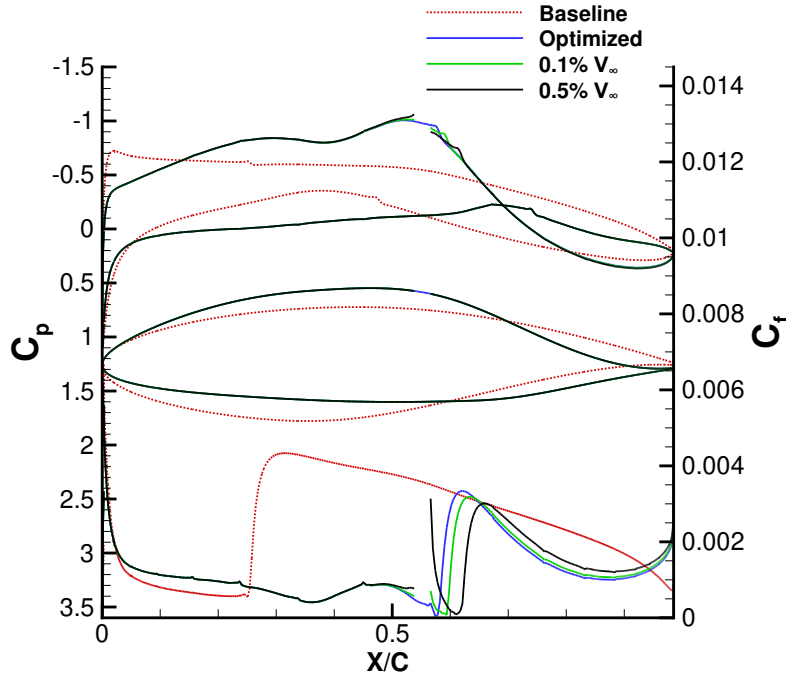| Configuration	C_D (counts)	L/D	AOA
Baseline	54.45	77.13	1.34°
Optimized	30.70 (-43.62%)	136.83	2.03°
$v_{\text{suc}} = 0.1\% \, V_\infty$	29.86 (-45.16%)	140.68	2.03°
$v_{\text{suc}} = 0.5\% \, V_\infty$	28.43 (-47.79%)	147.74	2.03°

Fig. 2   Pressure and lower-surface friction coefficient plots for cases involving the application of suction to the upper surface of an optimized geometry.

transition location, there is roughly a further 1.5% reduction in drag compared to just optimization alone. Increasing this suction velocity to $v_{\text{suc}} = 0.5\% \, V_\infty$, there is roughly a further 4% reduction in drag and the transition location is moved downstream to 62% of the chord, as shown in Figure 2.

3. Optimization with Fixed Suction Boundary Condition

Following the successful addition of suction at a single location at a suction speed of $v_{\text{suc}} = 0.1\% \, V_\infty$, as described in Section IV.A.1, an optimization of this airfoil was carried out to determine the extent of transition delay achieved by optimizing with suction applied, in contrast to the case described in the previous section where the airfoil is first optimized without suction. Table 3 shows that aerodynamic shape optimization with suction yielded a 43.9% drag reduction relative to the baseline geometry, compared to a 6.2% reduction from suction alone before optimization. Fig. 3 shows that the optimizer was able to successfully move the transition location further downstream. The results indicate that optimization in the presence of suction did not yield much additional drag reduction compared to the optimization without suction. Additionally, Section IV.A.2 indicates that the application of suction at the new transition location of a previously optimized geometry yields a higher drag reduction compared to the optimization with suction applied at the transition location of the baseline geometry.

Table 3 **Summary of results for an airfoil optimization with suction speed of $v_{suc} = 0.1\% \, V_\infty$ applied at 21% of the upper surface. For these cases, the suction extent is fixed and the geometry is optimized without suction to minimize drag at fixed lift.**

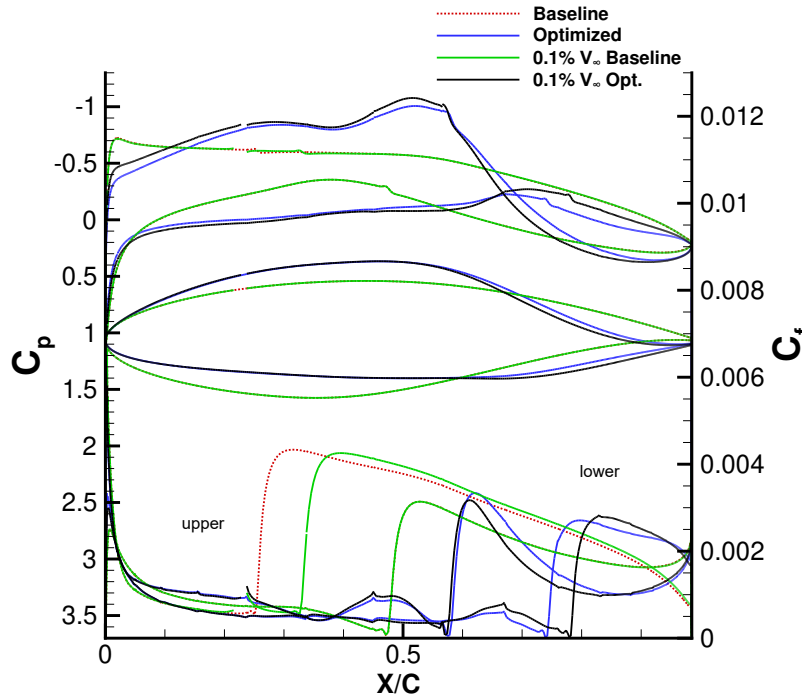| Configuration	C_D (counts)	L/D	AOA
Baseline	54.45	77.13	1.34°
Optimized	30.70 (-43.62%)	136.83	2.03°
Baseline with Suction	51.06 (-6.22%)	82.28	1.30°
Optimized with Suction	30.57 (-43.86%)	137.18	2.53°

Fig. 3 **Pressure and friction coefficient plots for cases involving the optimization of an airfoil with suction applied to the upper surface at $v_{suc} = 0.1\% \, V_\infty$**

B. Infinite Swept Wing Studies

The following infinite swept wing cases also use the RAE2822 airfoil as the initial geometry and were performed at $M = 0.78$, $Re = 15 \times 10^6$, $C_L = 0.492$, $\Lambda = 25°$. The computational meshes for these airfoils are again 300×122 O-grids.

1. Single Application of Suction Upstream of the Transition Location

Similarly to Section IV.A.1, a suitable location for suction was determined by solving the flow over the baseline geometry and trimming the wing to the target C_L. Following this, the suction boundary condition was applied 1.5% of the wing chord upstream of the transition location, with the suction extent spanning approximately 2% of the chord, and test was rerun, yielding a new transition location farther downstream. Three suction velocities were selected for this experiment, $v_{suc} = 0.1\% \, V_\infty$, $0.5\% \, V_\infty$ and $0.7\% \, V_\infty$. The last suction velocity was selected as an additional higher velocity compared with those used in IV.A.1, as this is a swept geometry which at these conditions, is more sensitive to crossflow instabilities than Tollmien-Schlichting instabilities and may require more active suction to suppress.

The results for the different configurations through which suction was applied are shown in Table 4. Figs. 4a - 4c

Table 4 Summary of results for infinite swept wing with suction. When applied to the upper surface, the suction extent is at 36% of the chord and when applied to the lower surface, the suction extent is at 20% of the chord. When applied on both the upper and lower surfaces, it uses both of the aforementioned locations on their respective surfaces.

Configuration	C_D (counts)	L/D	AOA
Baseline	55.23	89.08	1.48°
Upper Surface			
$v_{\text{suc}} = 0.1\% \, V_\infty$	53.43 (-3.26%)	92.08	1.45°
$v_{\text{suc}} = 0.5\% \, V_\infty$	52.25 (-5.40%)	94.26	1.41°
$v_{\text{suc}} = 0.7\% \, V_\infty$	53.14 (-3.78%)	92.59	1.42°
Lower Surface			
$v_{\text{suc}} = 0.1\% \, V_\infty$	52.89 (-4.24%)	93.02	1.48°
$v_{\text{suc}} = 0.5\% \, V_\infty$	50.87 (-7.89%)	96.72	1.48°
$v_{\text{suc}} = 0.7\% \, V_\infty$	50.72 (-8.17%)	97.00	1.48°
Both Surfaces			
$v_{\text{suc}} = 0.1\% \, V_\infty$	51.10 (-7.48%)	96.28	1.45°
$v_{\text{suc}} = 0.5\% \, V_\infty$	48.08 (-12.95%)	102.33	1.42°
$v_{\text{suc}} = 0.7\% \, V_\infty$	49.81 (-9.81%)	98.37	1.41°

show the pressure and friction coefficient plots. The transition location was determined to be at 36% of the chord on the upper surface and 20% of the chord on the lower surface, so the suction boundary condition was applied upstream of these locations. Fig. 4a uses the configuration with suction being applied to only the upper surface of the wing. When the suction velocity is 0.1% V_∞, transition is pushed downstream 5% of the chord with a 3.3% reduction in drag. When the suction velocity is increased to 0.5% V_∞, transition is pushed back 7% of the chord downstream with a 5.4% reduction in drag. One would expect this trend to continue, however upon increasing the suction velocity even further to 0.7% V_∞, the transition point is not translated further downstream as expected, compared with that when 0.5% V_∞ was used and the drag saw a smaller reduction as well, of 3.78%. This indicates that the increased suction velocity when applied to the upper surface increases the viscous drag and moves the transition location upstream. Fig. 4b applies the suction boundary condition on the lower surface of the wing, and even at a low suction velocity of 0.1% V_∞, the transition location was moved downstream 10% of the chord with a drag reduction of 4.2%. Increasing the suction velocity to 0.5% V_∞, there is a large drag reduction of 7.9% and the transition location is moved 18% of the chord downstream. When the suction velocity is increased to 0.7% V_∞, the amount of drag reduction is proportionally less at 8.2%; however it still results in a higher drag reduction and moves the transition location 20% downstream from the baseline model. When the suction boundary condition is applied to both the upper and lower surfaces upstream of their respective transition locations as in Fig. 4c, the expected results when using a suction velocity of 0.1% V_∞ result in a drag reduction of 7.5% and moves the transition location 5% downstream on the upper surface and 10% downstream on the lower surface. When the suction velocity is increased to 0.5% V_∞, the drag reduction is 13.0% and the transition location moves downstream 7% of the chord on the upper surface and 18% of the chord on the lower surface. When the suction velocity is increased to 0.7% V_∞, there is a smaller proportional drag reduction of 9.8%. The lower surface is able to move the transition location downstream to 20% of the chord while the upper surface struggles as per the results found in Fig. 4a where the suction boundary condition is applied only to the upper surface. This results in the net drag reduction being proportionally lower for the case when the suction velocity is 0.7% V_∞ compared with the results when the suction velocity is 0.5% V_∞.

2. Application of Suction to an Optimized Geometry

The suction boundary condition was also applied at a fixed location to a geometry optimized without suction. A lift-constrained drag minimization was performed with minimum thickness constraints enforced at each FFD volume

(a) Pressure and upper surface friction coefficient plot

(b) Pressure and lower surface friction coefficient plot

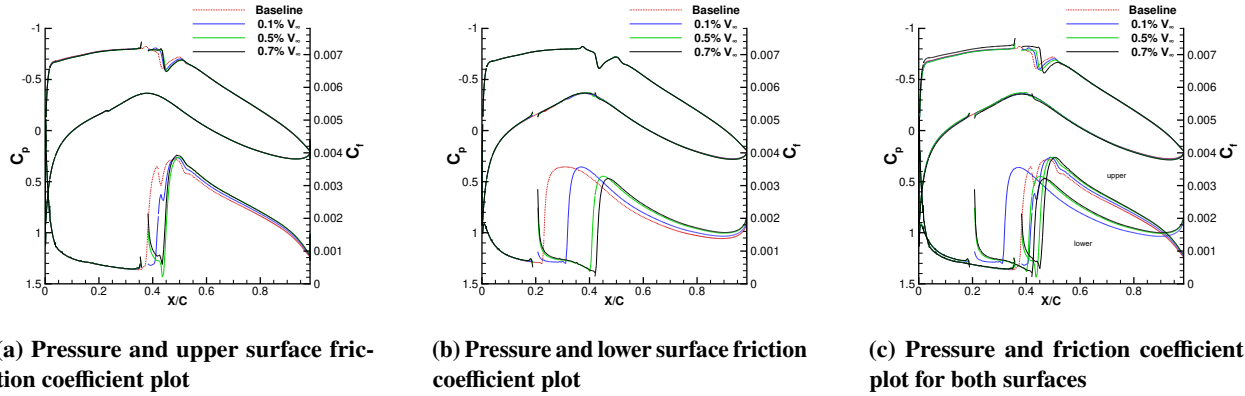**(c) Pressure and friction coefficient plot for both surfaces**

Fig. 4 Pressure and friction coefficient plots for the application of suction applied at 36% of the wing chord on the upper surface and 20% of the wing chord on the lower surface for their respective cases, for varying suction speeds.

control point pair and a minimum wing volume constraint. The chord length, leading edge and trailing edge of the airfoil are fixed while the angle of attack and section shape are allowed to vary. The optimization problem can be summarized as

$$\min_{\mathbf{X}} \quad C_D(\mathbf{X})$$
$$\text{s.t.} \quad C_L = 0.492$$
$$A \geq A_{\text{baseline}}$$
$$t/c \geq 0.15(t/c)_{\text{init}},$$

(7)

where $\mathbf{X}$ represents the design variable vector, C_L and C_D the lift and drag coefficients, respectively, C_L^* the target coefficient of lift, and t/c the thickness-to-chord ratio for each FFD control point pair. The 'init' subscript indicates the value of the quantity from the baseline geometry. The transition location of the optimized airfoil was determined and suction was applied upstream, in a method similar to Section IV.B.1. Table 5 shows that the optimized geometry has a 5.0% reduction in drag compared to the baseline design. While this drag reduction seems small compared to that found for the unswept geometry in Section IV.A.2, Piotrowski and Zingg found similar drag reductions and this was improved by increasing the streamwise grid resolution [29]. Figure 5 shows the pressure and friction coefficient plots, with both the upper and lower surfaces shown. Figure 5a shows that when a suction speed of $v_{\text{suc}} = 0.1\% \, V_{\infty}$ is applied to the upper surface, there is a drag reduction of 8.4% and the transition location is moved 5% further downstream. Similarly, when the suction boundary condition is applied to the lower surface at the same suction speed, the transition location moves downstream roughly 10% with a 7.0% reduction in drag. These results demonstrate that the application of suction to an optimized geometry provides further improvement over the case optimized without suction.

3. Optimization with Fixed Suction Boundary Condition

Following the successful application of suction to this swept geometry, the wing was then optimized using the same fixed suction boundary condition upstream of the transition location on the respective surfaces of the wing. This is to determine the effectiveness of both suction and aerodynamic shape optimization where suction is applied at the transition location of the baseline geometry, with the optimization problem being the same as in Section IV.B.2. The results for this optimization are shown in Table 6. The pressure and friction coefficient plots in Fig. 6 show that the optimizer was able to successfully move the transition location further downstream compared with cases that only used suction. When suction was applied to the upper surface, as in Fig. 6a, the transition point for the optimized geometry with suction moved downstream approximately 6% of the chord compared with the regular optimized geometry. The addition of suction also led to a 9.5% reduction in drag compared with the baseline geometry. Similarly in Fig. 6b, when suction is applied on the lower surface and the geometry is then optimized, the transition point moved downstream 8%

Table 5   Summary of results for flow evaluations with suction applied at 21% of the wing chord on the lower surface and 42% of the wing chord on the upper surface for their respective cases to an optimized geometry. For these cases, the suction extent is fixed and the suction speed is varied.

Configuration	C_D (counts)	L/D	AOA
Baseline	55.23	89.08	1.48°
Optimized	52.48 (-4.98%)	93.75	1.61°
Upper Surface			
$v_{\text{suc}} = 0.1\% \, V_\infty$	52.89 (-4.24%)	93.05	1.48°
$v_{\text{suc}} = 0.5\% \, V_\infty$	50.61 (-8.37%)	97.21	1.55°
Lower Surface			
$v_{\text{suc}} = 0.1\% \, V_\infty$	51.37 (-6.99%)	95.78	1.56°
$v_{\text{suc}} = 0.5\% \, V_\infty$	50.21 (-9.09%)	98.00	1.53°

(a) Suction applied to the upper surface

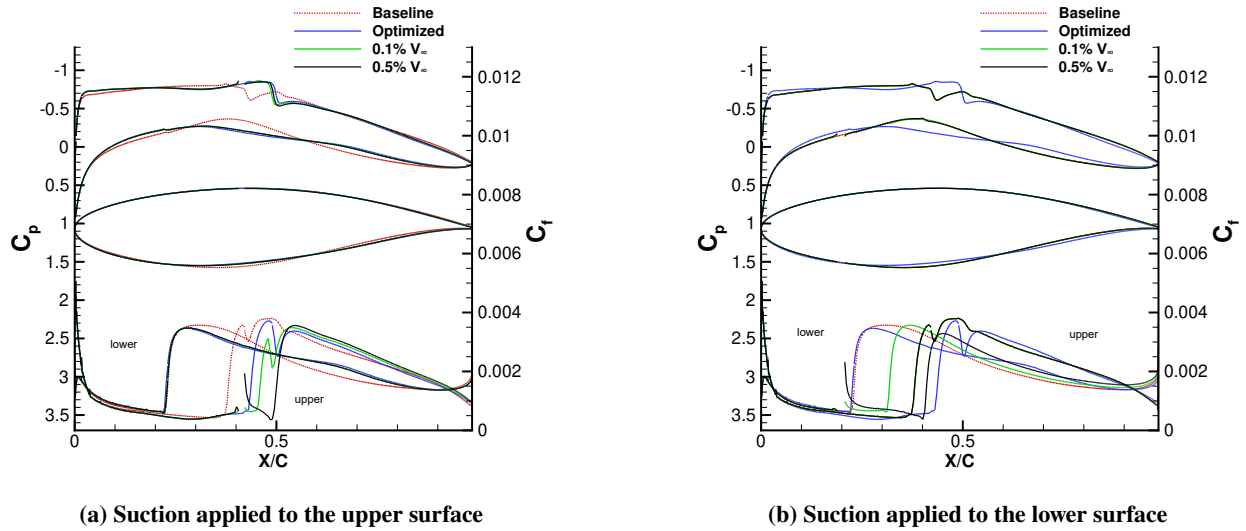**(b) Suction applied to the lower surface**

Fig. 5   Pressure and friction coefficient plots for cases involving the application of suction to the upper or lower surface of an optimized geometry. Suction is applied at 19% of the wing chord for the lower surface and at 42% of the wing chord for the upper surface for the respective cases while varying the suction speed.

of the chord when compared to the optimized geometry. Similar to the results found in Section IV.A, the optimization in the presence of suction yielded additional drag reduction compared to the optimization without suction. Additionally, Section IV.B.2 indicates that optimization with suction applied at the transition location of the baseline geometry yields a higher drag reduction compared to the application of suction at the new transition location of a previously optimized geometry.

4. Comparison of Baseline and Optimized Geometries with Different Suction Extents

The results in Sections IV.B.1 and IV.B.3 demonstrate that the transition point is moved downstream with an appropriate amount of suction. Here we consider the effect of the extent of the suction region, comparing a region spanning roughly 1.5% of the wing chord, as was used in the previous section, with a smaller extend of 0.5% of the wing chord; the results are shown in Table 7. The pressure and friction coefficient plots are shown in Fig. 7. The geometries are optimized with the suction location on the upper and lower surface remaining fixed and varying the suction extent upstream of the transition location, with the pressure and friction coefficient plots shown in Fig. 7. Fig. 7a

Table 6   Summary of results for infinite swept wing optimization with a suction speed of $v_{suc} = 0.1\%\ V_{\infty}$. Suction was applied to the upper surface at 36% of the chord and at 20% of the chord on the lower surface in their respective cases.

Configuration	C_D (counts)	L/D	AOA
Baseline	55.23	89.08	1.48°
Optimized	52.48 (-4.98%)	93.75	1.61°
Upper Surface			
Baseline with Suction	53.43 (-3.26%)	92.08	1.45°
Optimized with Suction	49.97 (-9.58%)	98.44	1.53°
Lower Surface			
Baseline with Suction	52.89 (-4.24%)	93.02	1.48°
Optimized with Suction	50.23 (-9.05%)	97.95	1.55°
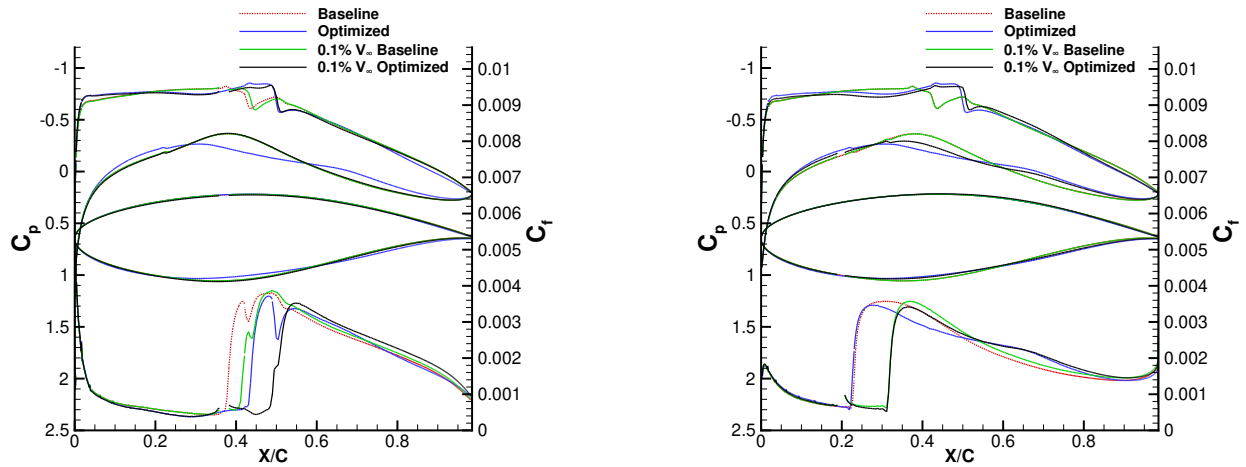
(a) Pressure and upper surface friction coefficient plot

(b) Pressure and lower surface friction coefficient plot

Fig. 6   Pressure and friction coefficient plots comparing the baseline and optimization cases with and without the suction boundary condition at a suction speed of $v_{suc} = 0.1\%\ V_{\infty}$. Suction is applied at 36% of the chord on the upper surface and at 20% of the chord on the lower surface for their respective cases.

shows the results for the optimization of the infinite swept wing with fixed suction locations on the upper surface. With 0.5%c upstream as the suction extent, the drag reduction is 7.7% and 1.0%c upstream of the transition location, the drag reduction found is 9.5%. In Fig. 7b, the wing with suction applied to the lower surface is optimized with suction extents of 0.5%c and 1.0%c upstream of the transition location, the drag reduction is 7.2% and 9.0% , respectively. These results indicate that while the application of suction to the upper surface did not yield a high amount of drag reduction on its own, when combined with aerodynamic shape optimization, it proved to yield a slightly higher drag reduction compared with the cases with suction on the lower surface. This indicates that much of the drag reduction stems from the aerodynamic shape optimization with the suction providing additional suppression of instabilities.

V. Conclusions

In this paper, we present a framework for aerodynamic shape optimization using active flow control through the use of suction to delay boundary-layer transition. This work includes airfoil and infinite swept wing lift-constrained drag minimization optimizations with fixed suction applications. In the case of the airfoil, flow evaluations and optimizations

Table 7   Results for the infinite swept wing optimization with suction at $v_{suc} = 0.1\%$ V_∞ at 36% of the chord on the upper surface and at 20% of the chord on the lower surface. The extent of the application of suction is 1% of the wing chord.

Configuration	C_D (counts)	L/D	AOA
Baseline	55.23	89.08	1.48°
Optimized	52.48 (-4.98%)	93.75	1.61°
Upper Surface			
Optimized with Suction	50.99 (-7.66%)	96.48	1.54°
Lower Surface			
Optimized with Suction	51.26 (-7.19%)	95.97	1.58°

(a) Suction applied on the upper surface

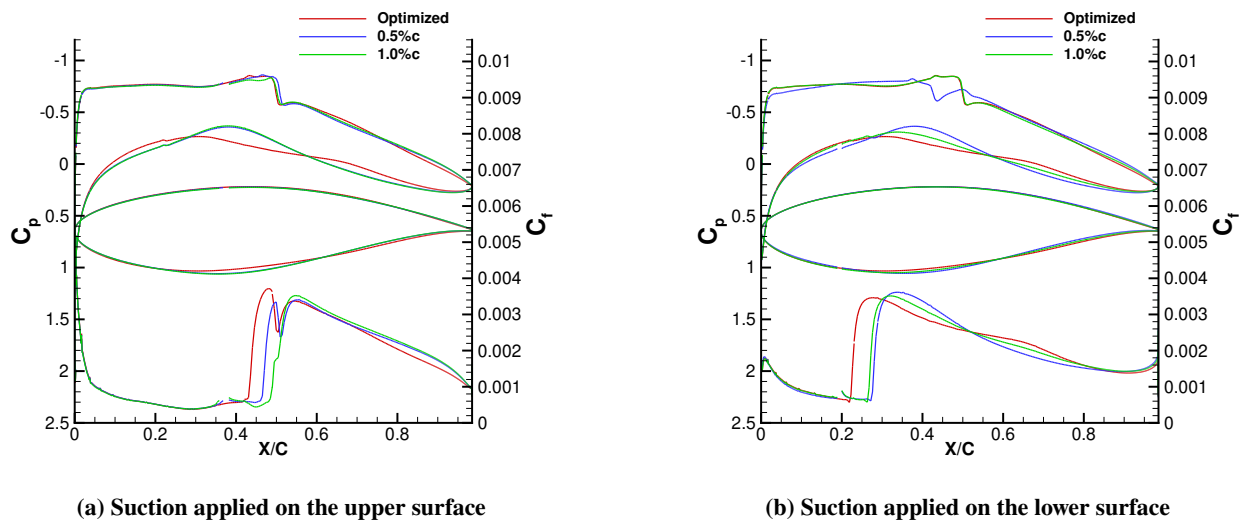(b) Suction applied on the lower surface

Fig. 7   Pressure and friction coefficient plot comparing the optimized geometry with suction applied at 36% of the chord on the upper surface and at 20% of the chord on the lower surface for their respective cases, while varying the size of the suction extent upstream of the transition location that the boundary condition is applied.

demonstrate that boundary-layer suction is capable of greatly suppressing Tollmien-Schlichting instabilities. A suction boundary condition was applied upstream of the transition location spanning roughly 2% of the airfoil chord at suction speeds of 0.1% V_∞ and 0.5% V_∞. By increasing the suction speed, there was an increase in the drag reduction and the transition location was moved further downstream. By adding a second suction location at this new transition location, further drag reductions were obtained, indicating the successful application of multiple suction locations at varying suction velocities. The airfoil was then optimized with suction at a speed of 0.1% V_∞ applied upstream of the baseline transition location, yielding a higher drag reduction compared to an airfoil optimized without the application of suction. These results indicate that the application of suction to a geometry optimized without suction present yields a higher drag reduction compared to the case where optimization is performed with a fixed suction location.

In the case of the infinite swept wing with fixed suction, the results demonstrate that boundary-layer suction, in combination with aerodynamic shape optimization, is able to adequately suppress crossflow instabilities and move the transition location downstream. Similar to the airfoil case, suction was applied upstream of the transition location and the geometry was then optimized. The results with suction yielded a higher drag reduction compared with those without the presence of suction. Compared with the case where suction is applied to a previously optimized geometry, the optimization with the suction boundary condition yielded a higher drag reduction, in contrast to the airfoil case. The results shown in this paper demonstrate that the approach to modelling suction and laminar-turbulent transition provides

13

a promising methodology for the future study and optimization of wings for hybrid laminar flow control.

References

[1] Rashad, R., and Zingg, D. W., "Aerodynamic shape optimization for natural laminar flow using a discrete-adjoint approach," *AIAA J.*, Vol. 54, No. 11, 2016, pp. 3321–3337.

[2] Bushnell, D., "Overview of aircraft drag reduction technology," *AGARD Report 786*, 1992.

[3] Green, J. E., "Civil aviation and the environmental challenge," *The Aeronautical Journal*, Vol. 107, No. 1072, 2003, pp. 281–299. https://doi.org/10.1017/S0001924000013579.

[4] Green, J. E., "Civil aviation and the environment – the next frontier for the aerodynamicist," *The Aeronautical Journal*, Vol. 110, No. 1110, 2006, pp. 469–486. https://doi.org/10.1017/S0001924000001378.

[5] Lynde, M. N., and Campbell, R. L., "Computational Design and Analysis of a Transonic Natural Laminar Flow Wing for a Wind Tunnel Model," *35th AIAA Applied Aerodynamics Conference*, American Institute of Aeronautics and Astronautics, Denver, Colorado, 2017. https://doi.org/10.2514/6.2017-3058.

[6] Lynde, M. N., Campbell, R. L., Rivers, M. B., Viken, S. A., Chan, D. T., Watkins, A. N., and Goodliff, S. L., "Preliminary Results from an Experimental Assessment of a Natural Laminar Flow Design Method," *AIAA Scitech 2019 Forum*, American Institute of Aeronautics and Astronautics, San Diego, California, 2019. https://doi.org/10.2514/6.2019-2298.

[7] Johansen, J., and Sørensen, J. N., "Prediction of Laminar/Turbulent Transition in Airfoil Flows," *Journal of Aircraft*, Vol. 36, No. 4, 1999, pp. 731–734. https://doi.org/10.2514/2.2501.

[8] Bobbitt, P. J., Ferris, J. C., Harvey, W. D., and Gordia, S. H., "Results for the Hybrid Laminar Flow Control Experiment," , No. NASA-TM-107582, 1992.

[9] Harvey, W. D., Harris, C. D., Brooks, C. W., Clukey, P. G., and Stack, J. P., "Design and Experimental Evaluation of a Swept, Supercritical LFC Airfoil," *Langley Symposium on Aerodynamics*, Vol. 1, 1986.

[10] Dagenhart, J. R., "Design of a Laminar-Flow-Control Supercritical Airfoil for a Swept Wing," *NASA, Langley Research Center, Hampton, VA, USA, CTOL Transport Technology*, 1978.

[11] Berry, S., Dagenhart, J. R., Brooks, C. W., and Harris, C. D., "Boundary-layer stability analysis of Langley Research Center 8-foot LFC experimental data," *NASA, Langley Research Center, Hampton, VA, USA, Research in Natural Laminar Flow and Laminar-Flow Control, Part 2*, 1987.

[12] Fisher, D. F., and Fischer, M. C., "Development flight tests of JetStar LFC leading-edge flight test experiment," *NASA, Langley Research Center, Research in Natural Laminar Flow and Laminar-Flow Control, Part 1*, 1987.

[13] Sudhi, A., Radespiel, R., and Badrya, C., "Design exploration of transonic airfoils for natural and hybrid laminar flow control applications," *J. Aircr.*, Vol. 60, No. 3, 2023, pp. 716–732.

[14] Osusky, M., and Zingg, D. W., "A parallel Newton-Krylov-Schur flow solver for the Navier-Stokes equations discretized using summation-by-parts operators," *AIAA Journal*, Vol. 51, No. 12, 2008, pp. 2833–2851.

[15] Osusky, M., Hicken, J., and Zingg, D., "A Parallel Newton-Krylov-Schur Flow Solver for the Navier-Stokes Equations Using the SBP-SAT Approach," *48th AIAA Aerospace Sciences Meeting Including the New Horizons Forum and Aerospace Exposition*, American Institute of Aeronautics and Astronautics, Orlando, Florida, 2010. https://doi.org/10.2514/6.2010-116.

[16] Piotrowski, M., and Zingg, D. W., "Investigation of a Local Correlation-based Transition Model in a Newton-Krylov Algorithm," *AIAA Scitech 2019 Forum*, American Institute of Aeronautics and Astronautics, San Diego, California, 2019. https://doi.org/10.2514/6.2019-2299.

[17] Piotrowski, M. G. H., and Zingg, D. W., "Smooth Local Correlation-Based Transition Model for the Spalart–Allmaras Turbulence Model," *AIAA Journal*, Vol. 59, No. 2, 2021, pp. 474–492. https://doi.org/10.2514/1.J059784.

[18] Hicken, J. E., and Zingg, D. W., "Aerodynamic Optimization Algorithm with Integrated Geometry Parameterization and Mesh Movement," *AIAA Journal*, Vol. 48, No. 2, 2010, pp. 400–413. https://doi.org/10.2514/1.44033.

[19] Gill, P. E., Murray, W., and Saunders, M. A., "SNOPT: An SQP Algorithm for Large-Scale Constrained Optimization," *SIAM Journal on Optimization*, Vol. 12, No. 4, 2002, pp. 979–1006. https://doi.org/10.1137/S1052623499350013.

[20] Gagnon, H., and Zingg, D. W., "Two-Level Free-Form and Axial Deformation for Exploratory Aerodynamic Shape Optimization," *AIAA Journal*, Vol. 53, No. 7, 2015, pp. 2015–2026. https://doi.org/10.2514/1.J053575.

[21] Del Rey Fernández, D. C., Hicken, J. E., and Zingg, D. W., "Simultaneous Approximation Terms for Multi-dimensional Summation-by-Parts Operators," *Journal of Scientific Computing*, Vol. 75, No. 1, 2018, pp. 83–110. https://doi.org/10.1007/s10915-017-0523-7.

[22] Piotrowski, M. G., and Zingg, D. W., "Investigation of a Smooth Local Correlation-based Transition Model in a Discrete-Adjoint Aerodynamic Shape Optimization Algorithm," *AIAA SCITECH 2022 Forum*, American Institute of Aeronautics and Astronautics, San Diego, CA & Virtual, 2022. https://doi.org/10.2514/6.2022-1865.

[23] Langtry, R. B., and Menter, F. R., "Correlation-Based Transition Modeling for Unstructured Parallelized Computational Fluid Dynamics Codes," *AIAA Journal*, Vol. 47, No. 12, 2009, pp. 2894–2906. https://doi.org/10.2514/1.42362.

[24] Spalart, P. R., and Allmaras, S. R., "A one-equation turbulence model for aerodynamic flows," *La Recherche Aerospatiale*, , No. 1, 1994, pp. 5–21.

[25] Piotrowski, M., and Zingg, D., "Compressibility corrections to extend a smooth local correlation-based transition model to transonic flows," *The Aeronautical Journal*, Vol. 127, No. 1313, 2023, pp. 1141–1170. https://doi.org/10.1017/aer.2022.105.

[26] Jameson, A., Martinelli, L., and Pierce, N. A., "Optimum aerodynamic design using the Navier-stokes equations," *Theor. Comput. Fluid Dyn.*, Vol. 10, No. 1-4, 1998, pp. 213–237.

[27] Osusky, L., and Zingg, D., "A novel aerodynamic shape optimization approach for three-dimensional turbulent flows," *50th AIAA Aerospace Sciences Meeting including the New Horizons Forum and Aerospace Exposition*, American Institute of Aeronautics and Astronautics, Reston, Virigina, 2012.

[28] Pulliam, T. H., and Zingg, D. W., *Fundamental Algorithms in Computational Fluid Dynamics*, Scientific Computation, Springer, New York, 2014.

[29] Piotrowski, M. G., and Zingg, D. W., "Investigation of a Smooth Local Correlation-based Transition Model in a Discrete-Adjoint Aerodynamic Shape Optimization Algorithm," *AIAA SCITECH 2022 Forum*, American Institute of Aeronautics and Astronautics, 2022. https://doi.org/10.2514/6.2022-1865, URL http://dx.doi.org/10.2514/6.2022-1865.